Available online at www.sciencedirect.com
ScienceDirect
Trans. Nonferrous Met. Soc. China 33(2023) 1677−1686
Transactions of Nonferrous Metals Society of China
www.tnmsc.cn

Effect of scanning speed on microstructure and texture of laser surface remelted 1050 Al alloy

Cheng-quan ZHANG[1], Lin-jiang CHAI[1], Qi-qi LI[1], Yan-long MA[1], Hui WANG[2], Xu-guang AN[2]

1. College of Materials Science and Engineering, Chongqing University of Technology, Chongqing 400054, China;
2. Interdisciplinary Materials Research Center, Institute for Advanced Study, Chengdu University, Chengdu 610106, China

Received 15 January 2022; accepted 16 August 2022

Abstract: A typical commercial Al alloy (1050) sheet was subjected to laser surface remelting (LSR) treatment at 400 W and different scanning speeds (2 and 8 mm/s), with dedicated microstructural and textural characterization made for original and LSRed specimens by using multiple characterization techniques. Results show that the as-received material has a typically recrystallized structure consisting of near-equiaxed grains (average grain size (20.4±15.4) μm) and many submicron second phase particles (SPPs). After the LSR treatment, remelting layers of the 2 mm/s and 8 mm/s specimens are mainly composed of columnar grains (with dense fine SPPs inside them), which are coarser than the near-equiaxed grains in the substrate. As the laser scanning speed increases from 2 to 8 mm/s, the depth of the remelted layer is evidently reduced, with the average width of the columnar grains decreasing from (38.0±4.3) to (33.9±2.0) μm. Meanwhile, the SPPs inside grains are significantly refined with largely increased number density. The LSR does not change the main textural characteristic ({100}⟨001⟩ cube component) of the as-received sheet but leads to the significantly increased textural intensity.

Key words: aluminum alloy; laser surface remelting; microstructure; texture; scanning speed; hardness

1 Introduction

Thanks to their advantageous properties like high specific strength, high electrical and thermal conductivity, good formability, and low cost, Al alloys have found wide applications in aero-space, transportation, and military industries [1−4]. Nevertheless, the intrinsically high chemical activity of Al often leads to the matrix of Al alloys to be preferably corroded as an anode (pitting corrosion) when there present other metallic elements [5]. To date, researchers have performed surface modifications for Al alloys by a variety of surface treatment methods like electroplating, electroless plating, thermal spraying, anodic oxidation, and vapor deposition, with many valuable results already well documented. It has to be admitted that these conventional methods usually have some drawbacks, i.e. high risk of environmental pollution for electroplating and electroless plating, low bonding strength between coating and substrate for thermal spraying, and limited thickness of modification layers produced by anodic oxidation and vapor deposition, making them unable to meet application requirements under harsh service conditions.

In recent years, along with sufficient under-standing of laser generation mode and the development of high-power laser, utilizing a laser to repair or harden surfaces of metallic materials has become a hot research topic in the field of surface

Corresponding author: Lin-jiang CHAI, Tel: +86-23-62563178, E-mail: chailinjiang@cqut.edu.cn
DOI: 10.1016/S1003-6326(23)66213-2
1003-6326/© 2023 The Nonferrous Metals Society of China. Published by Elsevier Ltd & Science Press

engineering. Compared to conventional surface modification techniques, laser surface treatment has many unique advantages including great operation (non-contact) feasibility, high processing efficiency, and good metallurgical bonding between modified layers and the substrate [6,7]. There have been some preliminary studies of effects of laser surface remelting (LSR) on corrosion resistance of Al alloys, with considerably improved pitting and stress corrosion resistance reported after appropriate LSR treatments [8−12]. For example, LI et al [11] found that coarse Al_2CuMg compounds could be essentially eliminated in the LSRed 2024-T351 Al alloy, which allowed its severe intergranular corrosion to be largely alleviated. RAO et al [12] figured out that the corrosion rate of 7075-T651 Al alloy would be reduced by four times after LSR, which was attributed to the disappearance of detrimental compounds in the LSRed layer. These studies have verified the ability of LSR to enhance the surface performances (especially corrosion resistance) of Al alloys. However, it is worthwhile noting that most of such studies mainly focus on establishing relationships between laser processing parameters and surface properties, yet with very limited attention paid to detailed microstructural and textural features induced by the LSR. In fact, insufficient understanding of such features does not allow in-depth surface modification mechanisms to be fully clarified.

In this work, therefore, a typical commercial 1050 Al alloy (with wide industrial applications) was subjected to LSR by an Nd:YAG pulsed laser device at two different scanning speeds (2 and 8 mm/s), with dedicated microstructural and textural characterizations performed for the specimens with and without the LSR. In addition, surface hardness variations of the LSRed specimens were probed and correlated with the revealed microstructural features. Results documented in this study should be able to facilitate better understanding of microstructure-based surface modification reasons of Al alloys after the LSR.

2 Experimental

2.1 Experimental materials

The as-received experimental material was an annealed 1050 Al alloy sheet (3 mm in thickness) with its chemical composition shown in Table 1.

Table 1 Chemical composition of 1050 Al alloy (wt.%)

Fe	Si	Mn	Cu	Mg	Zn	Ti	Al
0.244	0.046	<0.05	<0.05	<0.05	<0.05	0.027	Bal.

2.2 Laser surface remelting experiment

Rectangular specimens with dimensions of 15 mm × 10 mm × and 3 mm were cut from the as-received sheet along rolling, transverse and normal directions (RD, TD and ND), respectively. Their surfaces were polished with SiC abrasive papers and washed by anhydrous ethanol to remove oxides and contaminants. Then, under argon atmosphere, RD−TD surfaces of these specimens were LSRed with an Nd:YAG laser device (HWLW−600A−C−V5.2.01). The selected average laser power was 400 W and two scanning speeds (2 and 8 mm/s) were used, corresponding to linear energy densities of 200 and 50 J/mm, respectively. Other laser processing parameters include a defocus amount of 2 mm, a frequency of 20 Hz, a pulse duration of 5 ms, and an overlap rate of 50%. Although cooling rates experienced by the laser-treated surfaces were not directly measured, they could be roughly estimated to be 10^3−10^4 K/s according to literature with similar laser processing parameters [13−15].

2.3 Characterization methods

RD−TD surfaces of the as-received and the LSRed specimens were subjected to the X-ray diffraction (XRD, PANalytical Empyrean Series 2) examination with Cu K_α radiation at 40 kV and a scanning step size of 0.013° (2θ ranging from 30° to 80°). Jade 6.5 software was then used for post-processing and analyzing the XRD data. Detailed microstructural features of their cross sections (RD−ND surfaces) were characterized using a field emission scanning electron microscope (Zeiss sigma HD) equipped with an electron backscattered diffraction (EBSD) system and an energy dispersive spectrometer (EDS). The EBSD system included an Oxford instrument Nordlys-Max^2 detector and AZtec 3.1 software for data acquisition, and HKL Channel 5 software for data post-processing. Electron channeling contrast imaging (ECCI) technique based on backscattered electrons was mainly used to conduct direct microstructural observations of the specimens with and without the LSR. In addition, a Vickers hardness tester (HVS−Z1000) was used to measure

hardness variations on their cross sections (RD−ND surfaces). Measurements along five parallel paths (the thickness direction) were made for each specimen, with an interval of 100 μm between neighboring points in each measuring path. During the hardness test, a load of 100 g and a dwelling time of 10 s were used. Before the above characterizations and examinations, the to-be-analyzed specimen surfaces were ground by SiC abrasive papers (up to 5000#) and then electro-polished in a mixed solution of 10 mL perchloric acid and 90 mL methanol at 20 V and −30 °C for 60−70 s.

3 Results and discussion

Figure 1 presents the XRD patterns of the as-received and the LSRed specimens. One can see that the main phase in all the specimens is always the Al phase with the face centered cubic (FCC) structure, with very weak diffraction peaks corresponding to the α-(AlFeSi) phase. The Al diffraction peaks of the as-received specimen correspond to (111), (200), (220), and (311) planes in their sequence. After the LSR, intensities of major diffraction peaks are hardly changed (except slightly strengthening of the minor (111) peak), indicating that their phase constitutions and textural characteristics should have not changed markedly.

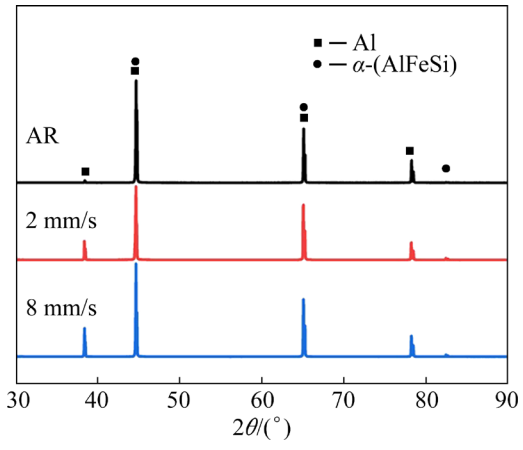

Fig. 1 XRD patterns of as-received (AR) and LSRed specimens

Figure 2 shows ECCI observations of the as-received specimen, from which its starting microstructure is found to be mainly composed of near-equiaxed grains with relatively uniform size (~20 μm on average). In addition, there exist a number of submicron second phase particles (SPPs) dispersed inside grains or at grain boundaries. After EDS mapping analyses (Fig. 3), they are found to be particularly enriched in Fe and Si. Again referring to Fig. 1, one can confirm that they correspond to the α-(AlFeSi) phase, which is consistent with previous reports on identifying typical SPPs in such an Al alloy [16].

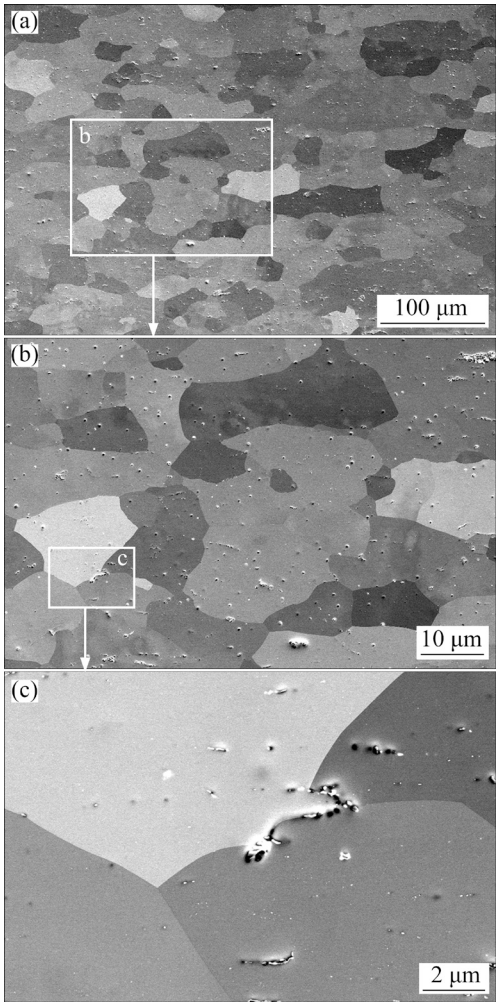

Fig. 2 ECCI observations of as-received specimen at different magnifications

Figure 4 shows EBSD characterization results of the as-received specimen and Fig. 4(a) (band contrast (BC) map) reveals near-equiaxed grains, consistent with the ECCI observation in Fig. 2. Figure 4(b) presents an inverse pole figure (IPF) map with high-angle grain boundaries (HAGBs, θ>15°) and low-angle grain boundaries (LAGBs, 3°<θ<15°) delineated by black and gray lines, respectively. Clearly, most grains are found to be separated by HAGBs and the orientation (color) inside each grain is generally uniform with hardly any LAGBs. By using the linear intercept method,

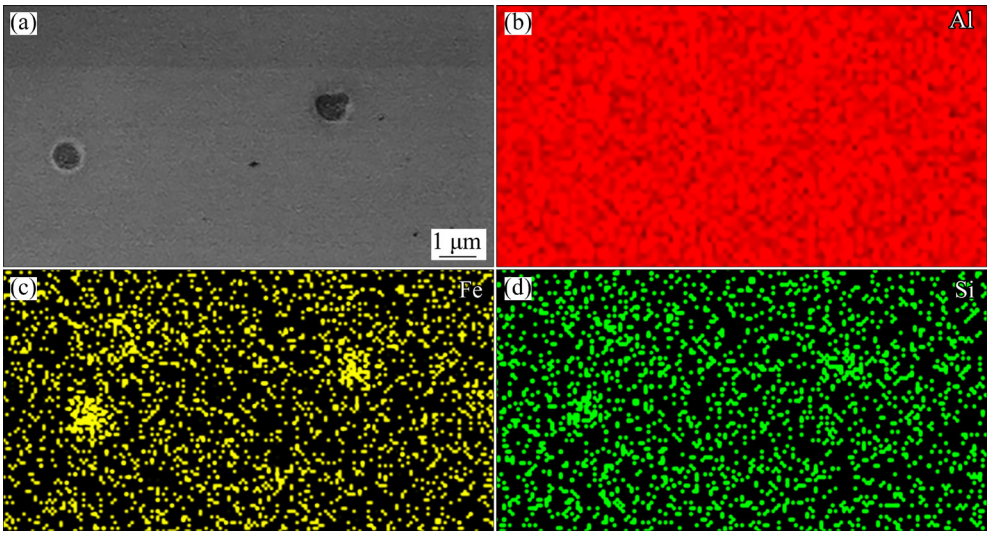

Fig. 3 EDS mapping results of typical SPPs in as-received specimen: (a) Morphological observation; (b−d) Distributions of Al, Fe, and Si elements, respectively

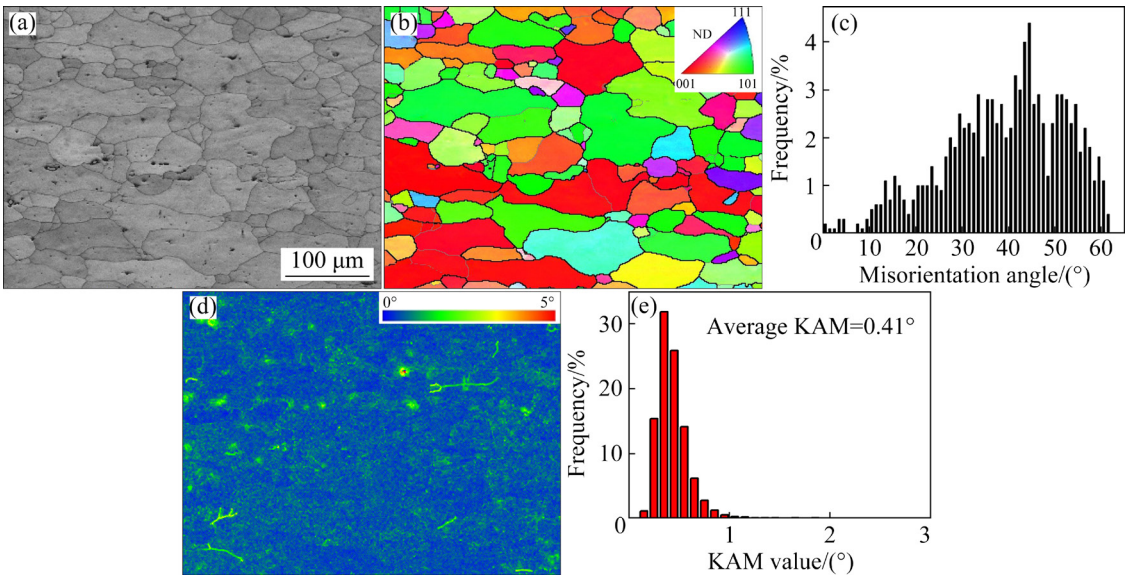

Fig. 4 EBSD characterization results (step size 1.0 μm) of as-received specimen: (a) BC map; (b) IPF map with black and gray lines representing HAGBs and LAGBs, respectively; (c) Misorientation angle distribution histogram; (d) KAM map; (e) KAM distribution histogram

their average grain size is determined to be (20.4±15.4) μm. Further, from misorientation angle distribution histogram (Fig. 4(c)), it is clearly revealed that the fraction of the HAGBs is much higher than that of the LAGBs, agreeing with the observation in Fig. 4(b). Figures 4(d) and (e) display kernel average misorientation (KAM) map and histogram, respectively. One can find that the KAM of the starting microstructure is generally small, with an average value of only 0.41°, suggesting hardly any stored energy [17]. From the above results, one can confirm that the as-received Al alloy has well recrystallized structure.

Figure 5 shows ECCI observations of the LSRed specimen at different scanning speeds (2 and 8 mm/s). Figures 5(a) and (d) reveal that both the LSRed specimens have a definite layer of remelting zone (RZ) featured by columnar grains, with their long axes deviated from the ND by some angles. The RZ depth in the 2 mm/s specimen is measured to be ~450 μm while it decreases to ~320 μm in the 8 mm/s specimen, demonstrating the effectiveness in reducing the laser-modified depth by increasing the scanning speed. Meanwhile,

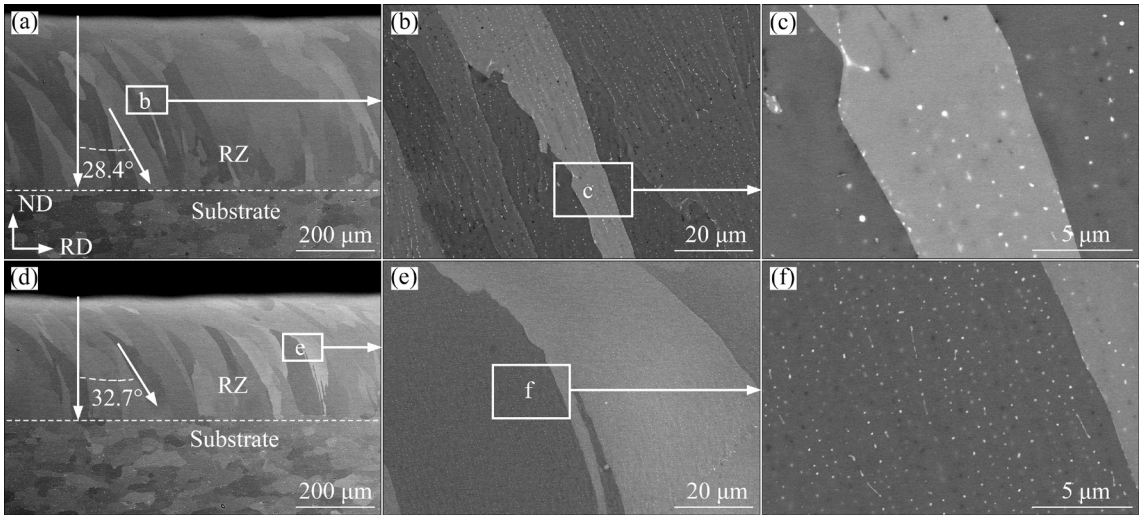

Fig. 5 Cross-sectional ECCI characterization results of LSRed specimens at different magnifications and different scanning speeds: (a−c) 2 mm/s; (d−f) 8 mm/s

the higher scanning speed also leads to larger deviation angles between the ND and the long axis of columnar grains. Previous studies [18] have demonstrated that with increasing scanning speed, the interaction time between the laser beam and the molten pool would be shortened and the energy input per unit time was also reduced, allowing only a shallower surface layer to be remelted. During subsequent cooling, the preferred growth direction (long axis) of columnar grains in the RZ is usually aligned along the maximum temperature gradient (towards the center of the laser beam) [19]. After increasing the moving speed of the laser beam, the columnar grains tended to deviate more from their initial growth direction (along the ND), leading to larger deviation angles between their long axes and the ND (Figs. 5(a) and (d)).

Further magnified observations (Figs. 5(b), (c), (e), and (f)) reveal that a large number of nanoscale precipitates exist inside the columnar grains and near their boundaries in the RZ of both the LSRed specimens, which should correspond to α-(AlFeSi) phase revealed in Fig. 1. With increasing the laser scanning speed, sizes of these precipitates seem to decrease markedly while their number density increases significantly. After quantitative analyses, the average size of such precipitates in the 2 mm/s specimen is (0.19±0.05) μm with a number density of 0.26 μm^{-2}. After raising the scanning speed to 8 mm/s, the average precipitate size goes down to (0.12±0.03) μm, and the number density increases to 1.04 μm^{-2}. These changes may be related to the decrease of energy input per unit volume during faster laser scanning that induces higher cooling rates in the molten pool. As a result, a greater undercooling could be produced in the solidification process, giving birth to more nucleation sites for the α-(AlFeSi) phase. Meanwhile, faster cooling would further suppress diffusion behaviors of alloying elements, eventually making these precipitates finer with a higher number density [20]. In addition, more grain nuclei could be produced by a larger solidification undercooling that should also be able to account for slightly reduced grain sizes in the 8 mm/s specimen (Fig. 5(d)).

Figure 6 shows the cross-sectional EBSD characterization results of the LSRed specimens. It is seen that the widths of the columnar grains in the RZ of the 2 mm/s specimen ((38.0±4.3) μm on average) are generally larger than those in the 8 mm/s specimen ((33.9±2.0) μm on average), both of which are larger than sizes of the near-equiaxed grains in the substrate (average size of (20.4±15.4) μm). A closer observation of Figs. 6(c) and (d) reveals that crystallographic orientations of many columnar grains in the RZ are exactly the same as near-equiaxed grains at the RZ/substrate interface (as indicated by arrows), suggesting these columnar grains to grow in an epitaxial way during the solidification. Recently, similar epitaxial grain growth has also been noted in an LSRed Inconel 718 alloy [21]. Figures 6(e) and (f) show the misorientation angle distribution histograms corresponding to the boxed regions in Figs. 6(a) and

(b), respectively. One can see that a certain amount of LABs appear in the RZs of two LSRed specimens, which may be related to the dislocation rearrangement induced by thermal stresses during laser processing [22].

Figures 7(a) and (b) present cross-sectional KAM maps of two LSRed specimens, from which the KAM is found to be relatively uniform in their RZs and there is no marked difference from the substrate. Figures 7(c) and (d) show that the average

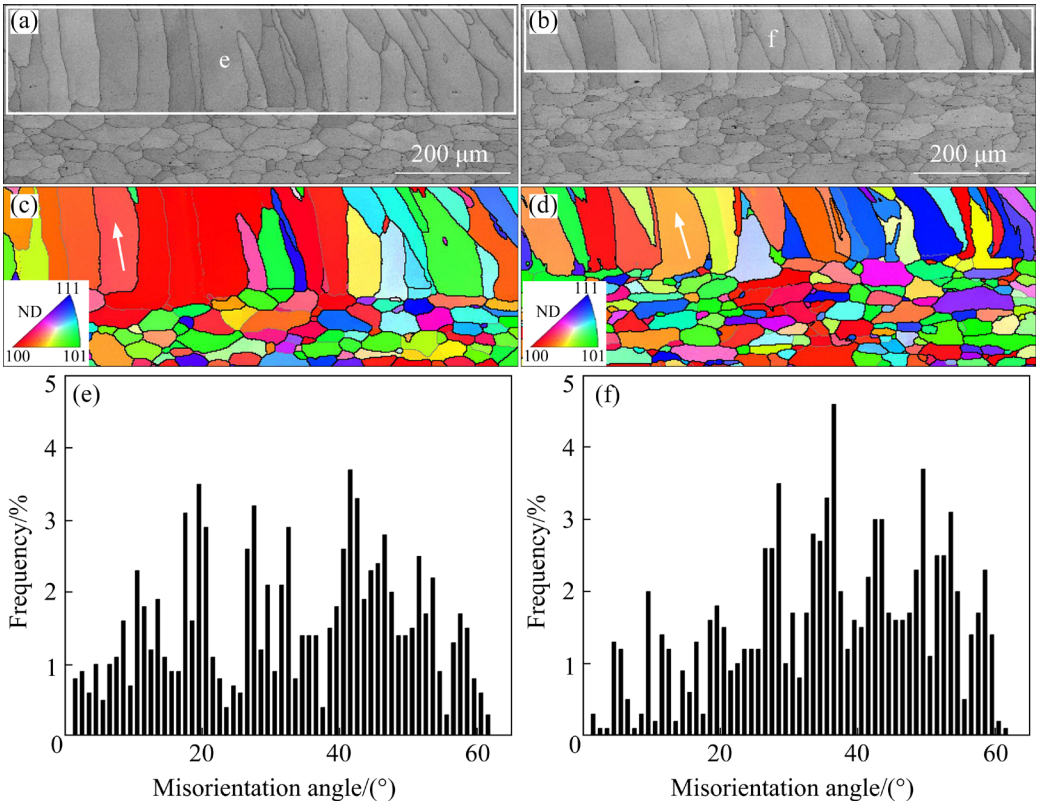

Fig. 6 Cross-sectional EBSD characterization (step size 2.0 μm) results of LSRed specimens: (a, c, e) BC map, IPF map, and misorientation angle distribution histogram of 2 mm/s specimen, respectively; (b, d, f) BC map, IPF map and misorientation angle distribution histogram of 8 mm/s specimen, respectively

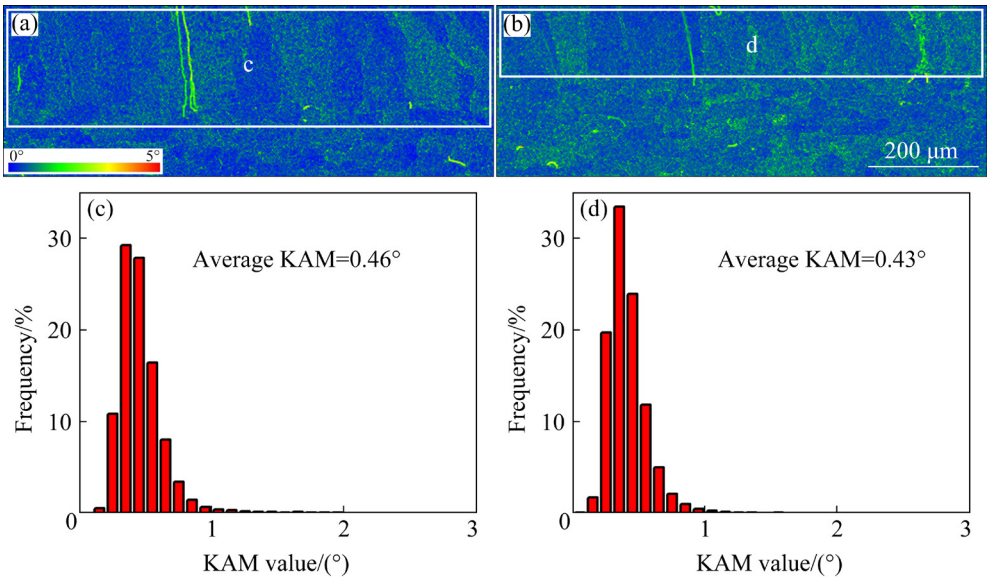

Fig. 7 (a, b) KAM maps corresponding to Figs. 6(a) and (b), respectively; (c, d) KAM distribution histograms corresponding to boxed regions (RZ) in (a) and (b), respectively

KAM value in the RZ of the 2 mm/s specimen is 0.46°, while that of the 8 mm/s specimen is 0.43°, just slightly higher than that of the substrate (0.41°). This suggests that very limited residual strains have been introduced into the surface layer by the LSR, despite high heating/cooling rates.

Figure 8 shows the crystallographic textural characteristics (pole figures) of the LSRed and as-received specimen surfaces. Figure 8(a) shows that the as-received specimen is mainly featured by the cube texture {100}⟨001⟩ [23] with a textural intensity of 5.2. After the LSR, although there appear some scattered orientations on the specimen surface, cube texture remains the main textural component and its intensity is even increased significantly. The textural intensity of the 2 mm/s specimen reaches 17.3, more than twice that of the as-received specimen. After increasing the laser scanning speed to 8 mm/s, the textural intensity decreases to 9.3, still higher than that of the as-received specimen. As mentioned above, epitaxial grain growth occurs in both the LSRed specimens, that is, some columnar grains in their RZs directly grow from the preexisting near-equiaxed grains in the substrate, making them have exactly the same orientation (Figs. 6(c) and (d)). In a recent study, similar findings have also been found in the RZ of an LSRed CoCrNi medium entropy alloy [24]. Since most of the equiaxed grains in the substrate have the cube orientation, such orientation will be naturally retained by the columnar grains developed through epitaxial growth in the RZ, allowing the original cube textural component to be maintained and even intensified. After the laser scanning speed increases from 2 to 8 mm/s, a larger undercooling can be induced by the higher cooling rate, which will produce more nucleation sites in the RZ during solidification. This means that more independent nuclei (not relying on the epitaxial growth) can be generated directly in the RZ region. On the one hand, this can lead to effective grain refinement in the RZ (Figs. 6(a) and (b)); on the other hand, more non-cube orientation grains will be generated, leading to the decreased textural intensity compared to the 2 mm/s specimen (Figs. 8(b) and (c)). In other

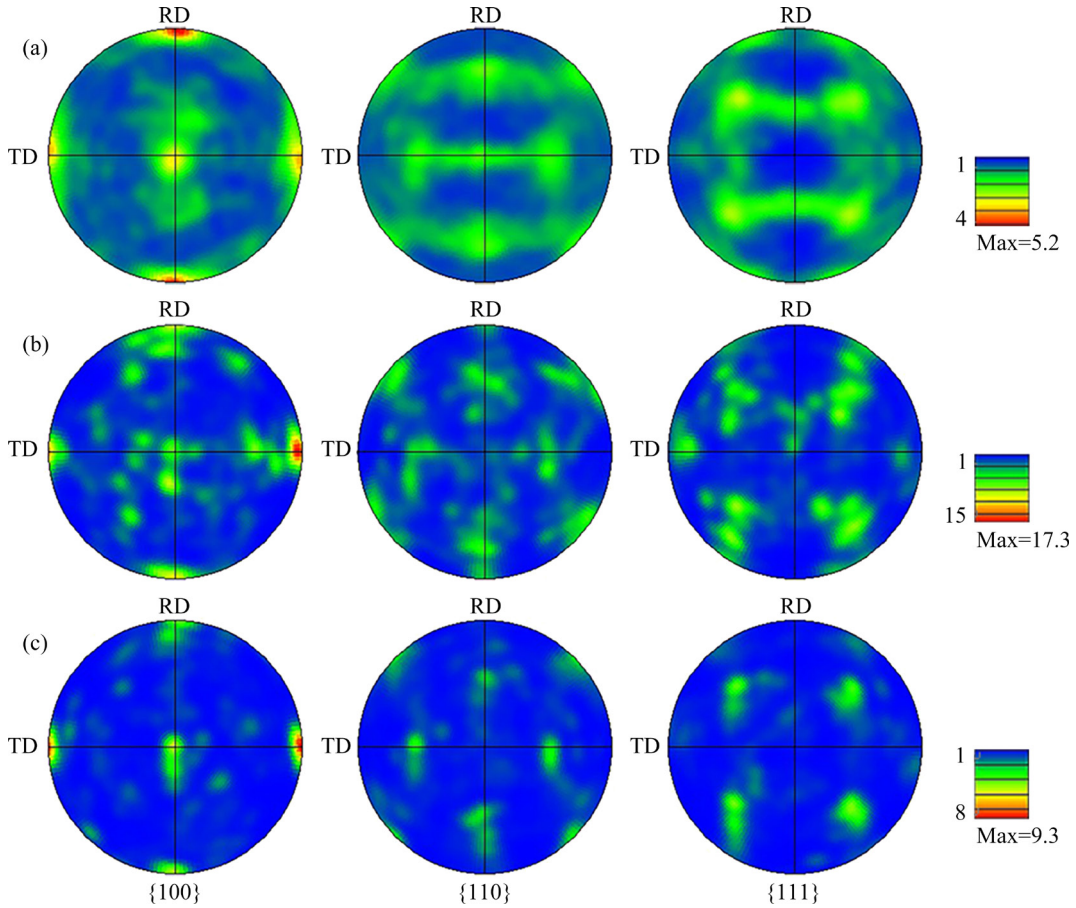

Fig. 8 Pole figures (each corresponding to a scanning area of 0.12 mm^2) of as-received (a), 2 mm/s (b) and 8 mm/s (c) specimens

words, regarding the specific effect of the laser scanning speed, one can consider that the LSR is capable of intensifying surface textures of the 1050 Al alloy and such an effect is further intensified after reducing the scanning speed from 8 to 2 mm/s.

Figure 9 shows hardness test results on the cross-sections of the LSRed specimens. Surface hardnesses of both the LSRed specimens are found to be slightly lower than that of the substrate (HV (24.1±0.2)). In fact, the surface hardness (HV (24.1±0.3)) of both the LSRed specimens is almost identical to that of the initial specimen, suggesting that it is hardly affected by the LSR. The average hardnesses of the RZs of the 2 mm/s and the 8 mm/s specimens are determined to be HV (21.8±0.4) and HV (23.1±0.5), respectively. The above mircrostructrual characterization reveals that the surface grains of the LSRed specimen are coarser than those of the substrate, which may be one main factor accounting for the hardness variation. The Hall−Petch relation can be expressed as [25]

$$\Delta HV_{\mathrm{HP}} = k_{\mathrm{HV}}(d_{\mathrm{M}}^{-0.5} - d_{\mathrm{RZ}}^{-0.5}).$$

where ΔHV_{HP} is the hardness change due to grain size difference, k_{HV} is the Hall−Petch slope in the unit of Vickers hardness (the k_{HV} of Al is ~13.7 HV·μm$^{0.5}$ at room temperature [26]), and d_{M} and d_{RZ} are average grain sizes of the substrate and the RZ, respectively. The calculation results are listed in Table 2, which also displays the hardness difference measured experimentally between the RZ and the substrate.

From Table 2, one can see that for both the LSRed specimens, there are some deviations

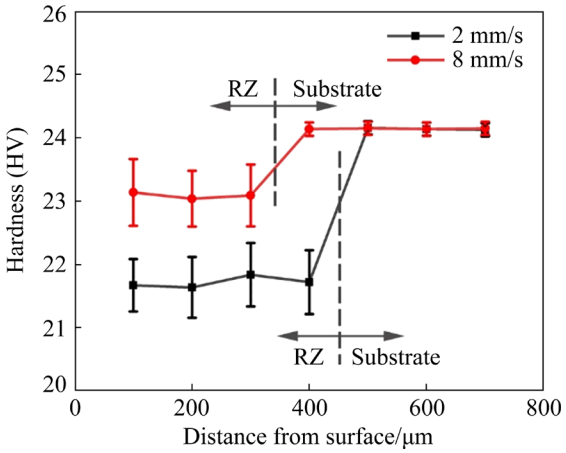

Fig. 9 Cross-sectional hardness variations of LSRed specimens at different laser scanning speeds

Table 2 Measured and calculated hardness differences between RZ and substrate

Specimen	$\Delta HV_{\mathrm{T}}^{\mathrm{a}}$	$\Delta HV_{\mathrm{HP}}^{\mathrm{b}}$
2 mm/s	2.3	0.8
8 mm/s	1.0	0.7

[a] Measured total hardness difference compared to that of the substrate; [b] Relative hardness contribution from the Hall−Petch effect

between the calculated and the experimentally measured results, suggesting that there must be some other influential factors in addition to grain size. After comparing Figs. 2 and 5, it is found that the RZs of both the LSRed specimens contain high-density fine precipitates, which should be more effective to hinder dislocation movement than the coarser SPPs in the substrate [27,28]. In addition, Fig. 8 shows that the textural intensity of the specimen surface after the LSR has changed significantly compared to that of the substrate. This may also affect the hardness [29], but it is difficult to give more quantitative analyses at present. Note that although the 1050 Al alloy is softened after the LSR in this work, the hardness drop is relatively small (Fig. 9), indicating that the changes of precipitates and texture have only a mild effect on its hardness. Previous studies demonstrated that the presence of dispersive fine precipitates is beneficial to suppressing pitting corrosion of Al alloys [30], and the strong cube texture is very helpful to improve its intergranular corrosion resistance [31]. Our results in the present work show that the LSR allows the Al alloy to obtain dispersive fine precipitates and stronger cube texture simultaneously, which may have accounted for the significantly improved corrosion resistance, as widely reported for LSRed Al alloys [32,33]. It is thus believed that our new findings about LSRed microstructural and textural features should be able to help other researchers reach a more comprehensive and in-depth understanding of surface modification mechanisms of LSRed Al alloys.

4 Conclusions

(1) The microstructure of the as-received 1050 Al alloy consists of near-equiaxed grains (average grain size (20.4±15.4) μm) and many submicron α-(AlFeSi) particles. After the LSR treatment at

400 W, RZs of the specimens are mainly composed of columnar grains (with dense fine SPPs inside them), which are coarser than the near-equiaxed grains in the substrate.

(2) When the laser scanning speed increases from 2 to 8 mm/s, the depth of RZ is evidently decreased, with the average width of the columnar grains decreasing from (38.0±4.3) to (33.9±2.0) μm. Meanwhile, the SPPs inside grains are significantly refined with largely increased number density.

(3) The LSR does not change the main textural characteristics ({100}⟨001⟩ cube texture) of the substrate, but the epitaxial growth of columnar grains in the RZ leads to the significantly increased textural intensity (from 5.2 for the as-received specimen to 17.3 after the 2 mm/s laser scanning).

(4) The surface hardnesses of the LSRed specimens decrease slightly, which can be attributed to the appearance of the relatively coarse columnar grains in the RZ. Such softening can be suppressed by increasing the laser scanning speed due to effective grain refinement.

Acknowledgments

The authors are grateful for the financial supports from the University Innovation Research Group of Chongqing, China (No. CXQT20023) and the Graduate Student Innovation Program of Chongqing University of Technology, China (No. CLGYCX20203006).

References

[1] GEORGANTZIA E, GKANTOU M, KAMARIS G S. Aluminium alloys as structural material: A review of research [J]. Engineering Structures, 2021, 227: 111372.

[2] CHI Y M, GU G C, YU H J, CHEN C Z. Laser surface alloying on aluminum and its alloys: A review [J]. Optics and Lasers in Engineering, 2018, 100: 23−37.

[3] LUO G Y, XIAO H, LI S M, WANG C S, ZHU Q, SONG L J. Quasi-continuous-wave laser surface melting of aluminium alloy: Precipitate morphology, solute segregation and corrosion resistance [J]. Corrosion Science, 2019, 152: 109−119.

[4] ZHANG J L, SONG B, WEI Q S, BOURELL D, SHI Y S. A review of selective laser melting of aluminum alloys: Processing, microstructure, property and developing trends [J]. Journal of Materials Science & Technology, 2019, 35: 270−284.

[5] JI Yuan-yuan, XU Yun-ze, ZHANG Bin-bin, BEHNAMIAN Y, XIA Da-hai, HU Wen-bin. Review of micro-scale and atomic-scale corrosion mechanisms of second phases in aluminum alloys [J]. Transactions of Nonferrous Metals Society of China, 2021, 31: 3205−3227.

[6] QUAZI M M, FAZAL M A, HASEEB A S M A, YUSOF F, MASJUKI H H, ARSLAN A. Laser-based surface modifications of aluminum and its alloys [J]. Critical Reviews in Solid State and Materials Sciences, 2016, 41: 106−131.

[7] SERCOMBE T B, LI X. Selective laser melting of aluminium and aluminium metal matrix composites: Review [J]. Materials Technology, 2016, 31: 77−85.

[8] WEI P, CHEN Z, ZHANG S Z, FANG X W, LU B H, ZHANG L J, WEI Z Y. Effect of T6 heat treatment on the surface tribological and corrosion properties of $AlSi_{10}Mg$ samples produced by selective laser melting [J]. Materials Characterization, 2021, 171: 110769.

[9] LEI X W, NUAM V L, YUAN Y X, BAI Y, YAO W J, WANG N. Investigation on laser beam remelted Al−Cu−Li alloy Part II: Corrosion behavior and mechanical properties [J]. Journal of Alloys and Compounds, 2021, 873: 159765.

[10] MA S C, ZHAO Y, ZOU J S, YAN K, LIU C. The effect of laser surface melting on microstructure and corrosion behavior of friction stir welded aluminum alloy 2219 [J]. Optics & Laser Technology, 2017, 96: 299−306.

[11] LI R, FERREIRA M G S, ALMEIDA A, VILAR R, WATKINS K G, MCMAHON M A, STEEN W M. Localized corrosion of laser surface melted 2024-T351 aluminium alloy [J]. Surface and Coatings Technology, 1996, 81: 290−296.

[12] RAO A C U, VASU V, SHARIFF S M, SRINADH K V S. Influence of diode laser surface melting on microstructure and corrosion resistance of 7075 aluminium alloy [J]. International Journal of Microstructure and Materials Properties, 2016, 11: 85−104.

[13] LI J, CHENG X, LI Z, ZONG X, ZHANG S Q, WANG H M. Improving the mechanical properties of Al−5Si−1Cu−Mg aluminum alloy produced by laser additive manufacturing with post-process heat treatments [J]. Materials Science and Engineering A, 2018, 735: 408−417.

[14] LIU T, ZHAN X H, KANG Y. The influence of thermal distribution on macro profile and dendrites morphology based on temperature field simulation of 6061 aluminum alloy laser welded joint [J]. Journal of Adhesion Science and Technology, 2020, 34: 2144−2160.

[15] LIU Y J, LIU Z, JIANG Y, WANG G W, YANG Y, ZHANG L. Gradient in microstructure and mechanical property of selective laser melted $AlSi_{10}Mg$ [J]. Journal of Alloys and Compounds, 2018, 735: 1414−1421.

[16] ZHANG Jing, PAN Fu-sheng, ZUO Ru-lin, WANG Wen-gao. Medium temperature phase transformation in AA1235 aluminium sheets for foils [J]. The Chinese Journal of Nonferrous Metals, 2006, 16: 1394−1399. (in Chinese)

[17] GUO N, LI D R, YU H B, XIN R I, ZHANG Z M, LI X X, LIU C, SONG B, CHAI L J. Annealing behavior of gradient structured copper and its effect on mechanical properties [J]. Materials Science and Engineering A, 2017, 702: 331−342.

[18] LI Y, ZALOŽNIK M, ZOLLINGER J, DEMBINSKI L, MATHIEU A. Effects of the powder, laser parameters and surface conditions on the molten pool formation in the selective laser melting of IN718 [J]. Journal of Materials Processing Technology, 2021, 289: 116930.

[19] PINEDA D A, MARTORANO M A. Columnar to equiaxed transition in directional solidification of inoculated melts [J]. Acta Materialia, 2013, 61: 1785−1797.
[20] PRIYA P, JOHNSON D R, KRANE M J M. Precipitation during cooling of 7××× aluminum alloys [J]. Computational Materials Science, 2017, 139: 273−284.
[21] CHAI Lin-jiang, YUAN Shan-shan, HUANG Wei-jiu, YANG Xu-sheng, WANG Fang-jun, WANG Dong-zhe, WANG Jun-jun. Microstructural characterization of Inconel 718 alloy after pulsed laser surface treatment at different powers [J]. Transactions of Nonferrous Metals Society of China, 2018, 28: 1530−1537.
[22] LIU H, NAKATA K, ZHANG J X, YAMAMOTO N, LIAO J. Microstructural evolution of fusion zone in laser beam welds of pure titanium [J]. Materials Characterization, 2012, 65: 1−7.
[23] ENGLER O. On the influence of orientation pinning on growth selection of recrystallisation [J]. Acta Materialia, 1998, 46: 1555−1568.
[24] CHAI L J, XIANG K, XIA J Y, FALLAH V, MURTY K L, YAO Z W, GAN B. Effects of pulsed laser surface treatments on microstructural characteristics and hardness of CrCoNi medium-entropy alloy [J]. Philosophical Magazine, 2019, 99: 3015−3031.
[25] DAI J H, XIA J Y, CHAI L J, MURTY K L, GUO N, DAYMOND M R. Correlation of microstructural, textural characteristics and hardness of Ti−6Al−4V sheet β-cooled at different rates [J]. Journal of Materials Science, 2020, 55: 8346−8362.
[26] HANSEN N. The effect of grain size and strain on the tensile flow stress of copper at room temperature [J]. Strength of Metals and Alloys, 1979, 2: 849−854.
[27] EL-ATY A A, XU Y, GUO X Z, ZHANG S H, MA Y, CHEN D Y. Strengthening mechanisms, deformation behavior, and anisotropic mechanical properties of Al−Li alloys: A review [J]. Journal of Advanced Research, 2018, 10: 49−67.
[28] WANG X, EMBURY J D, POOLE W J, ESMAEILI S, LLOYD D J. Precipitation strengthening of the aluminum alloy AA6111 [J]. Metallurgical and Materials Transactions A, 2003, 34: 2913−2924.
[29] FITZNER A, PALMER J, GARDNER B, THOMAS M, PREUSS M, DA FONSECA J Q. On the work hardening of titanium: New insights from nanoindentation [J]. Journal of Materials Science, 2019, 54: 7961−7974.
[30] SANTHOSH N, KEMPAIAH U N, GOWDA A C, RAGHU M S, SAJJAN G. Corrosion characterization of silicon carbide and fly ash particulates dispersion strengthened aluminium 5083 composites [J]. Journal of Catalyst and Catalysis, 2017, 4: 9−21.
[31] WU B L, SHI J H, ZHANG Y D, WANG Y N, ZUO L, ESLING C. The influence of texture and GBCD on stress corrosion and intergranular corrosion in 2024 aluminium alloy [J]. Solid State Phenomena, 2005, 105: 181−186.
[32] MROCZKOWSKA K M, ANTOŃCZAK A J, GĄSIOREK J. The corrosion resistance of aluminum alloy modified by laser radiation [J]. Coatings, 2019, 9: 672.
[33] GU X H, ZHANG J X, FAN X L, DAI N W, XIAO Y, ZHANG L C. Abnormal corrosion behavior of selective laser melted $AlSi_{10}Mg$ alloy induced by heat treatment at 300 °C [J]. Journal of Alloys and Compounds, 2019, 803: 314−324.

扫描速度对激光表面重熔 1050 铝合金显微组织和织构的影响

张成全[1]，柴林江[1]，李琪琪[1]，麻彦龙[1]，王 辉[2]，安旭光[2]

1. 重庆理工大学 材料科学与工程学院，重庆 400054；
2. 成都大学 高等研究院 跨学科材料研究中心，成都 610106

摘 要：在 400 W 激光功率和不同扫描速度(2 和 8 mm/s)下对典型商用铝合金(1050)板材进行激光重熔试验，并采用多种表征技术对激光重熔前后样品的显微组织及织构特征进行精细表征。结果表明，原材料铝合金具有典型的再结晶组织，由尺寸较均匀的近等轴晶(平均晶粒尺寸为(20.4±15.4) μm)和一些亚微米尺度的第二相颗粒共同组成。经 2 和 8 mm/s 的激光重熔加工后，样品表层均出现以柱状晶为主要组织特征(晶内存在亚微米级析出相)的重熔层，且明显较基体组织粗大。对比发现，当扫描速度从 2 升至 8 mm/s 时，重熔层深度明显降低，其内部柱状晶的平均宽度也由(38.0±4.3) μm 降至(33.9±2.0) μm。同时，晶内析出相也得到显著细化，而其数密度则大幅增加。激光表面重熔未改变 1050 铝合金的主要织构特征，即仍以{100}⟨001⟩立方织构为主，但织构强度明显增加。

关键词：铝合金；激光表面重熔；显微组织；织构；扫描速度；硬度

(Edited by Wei-ping CHEN)